21. A. Caviglia *et al.*, *Nature* **456**, 624 (2008).
22. M. Basletic *et al.*, *Nat. Mater.* **7**, 621 (2008).
23. W. Siemons *et al.*, *Phys. Rev. Lett.* **98**, 196802 (2007).
24. C. Cen *et al.*, *Nat. Mater.* **7**, 298 (2008).
25. J. M. Albina, M. Mrovec, B. Meyer, C. Elsasser, *Phys. Rev. B* **76**, 165103 (2007).
26. C. W. Schneider, S. Thiel, G. Hammerl, C. Richter, J. Mannhart, *Appl. Phys. Lett.* **89**, 122101 (2006).
27. See supporting material on *Science* Online.
28. Supported by NSF grant 0704022, Deutsche Forschungsgemeinschaft grant SFB 484, and the European Community NANOXIDE project.

Supporting Online Material
www.sciencemag.org/cgi/content/full/323/5917/1026/DC1
Figs. S1 to S8

10 November 2008; accepted 2 January 2009
10.1126/science.1168294

REPORTS

Macroscopic 10-Terabit–per–Square-Inch Arrays from Block Copolymers with Lateral Order

Soojin Park,[1]* Dong Hyun Lee,[1] Ji Xu,[1] Bokyung Kim,[1] Sung Woo Hong,[1] Unyong Jeong,[2] Ting Xu,[3]† Thomas P. Russell[1]†

Generating laterally ordered, ultradense, macroscopic arrays of nanoscopic elements will revolutionize the microelectronic and storage industries. We used faceted surfaces of commercially available sapphire wafers to guide the self-assembly of block copolymer microdomains into oriented arrays with quasi–long-range crystalline order over arbitrarily large wafer surfaces. Ordered arrays of cylindrical microdomains 3 nanometers in diameter, with areal densities in excess of 10 terabits per square inch, were produced. The sawtoothed substrate topography provides directional guidance to the self-assembly of the block copolymer, which is tolerant of surface defects, such as dislocations. The lateral ordering and lattice orientation of the single-grain arrays of microdomains are maintained over the entire surface. The approach described is parallel, applicable to different substrates and block copolymers, and opens a versatile route toward ultrahigh-density systems.

Producing a surface with an ultradense array of addressable nanoscopic elements that is perfectly ordered over macroscopic length scales is a formidable challenge. The self-assembly of block copolymers (BCPs), two chemically dissimilar polymers joined together, is emerging as a promising route to generate templates and scaffolds for the fabrication of nanostructured materials and offers a potential solution to this challenge (*1*–*3*). Despite the substantial advances that have been made to enhance the lateral ordering of the BCP microdomains in thin films, achieving perfect order over macroscopic length scales has not been possible (*4*–*7*). In thin films, BCPs self-assemble into grains, tens of microns in size, of laterally ordered nanoscopic microdomains. Electron beam (e-beam) lithography is a serial writing process, and although slow, has been successfully used to produce nanoscopic chemical or topographic surface patterns that can be used to guide the self-assembly of BCPs (*4*, *5*, *8*, *9*). However, even though the self-assembly of BCPs can correct errors in the patterns, perfect ordering over large areas has not yet been achieved. Nanoimprint lithography (*10*, *11*), on the other hand, is a parallel patterning process but requires a perfect master to replicate. We show that most of these limitations can be overcome by capitalizing on a well-established surface reconstruction of commercially available single-crystalline wafers to generate nanoscopic surface facets that can guide the self-assembly of BCPs into a highly ordered, single-grain array of nanoscopic elements with a well-defined orientation over large areas.

Large, defect-free single-crystalline wafers, such as silicon or sapphire, with a well-defined orientation of the crystal lattice are commercially available (*12*–*14*). By the cutting of single crystals along specific crystallographic planes, unstable surfaces can be produced that, upon heating, reconstruct, generating crystal facets that form a sawtooth topography, where the orientation of the ridges formed by the sawtooth persists over the entire surface (*13*, *14*). Sapphire (α-Al_2O_3), cut along the $(10\bar{1}0)$ or M plane, is used as an example, although the concept applies to other single-crystalline materials. The surface reconstruction is shown schematically in Fig. 1 along with atomic force microscopy (AFM) images of a freshly cut and a faceted sapphire surface (*13*, *14*). Initially the surface is featureless. Upon annealing, the surface reconstructs and crystalline facets form a sawtooth pattern on the surface. With the sapphire substrates used in this study, the pitch of the sawtooth was varied from 160 to 24 nm, with peak-to-valley heights or amplitudes ranging from 20 to 3 nm by being annealed in air at temperatures from 1300° to 1500°C for 24 hours [supporting online material (SOM), section S1]. Crystallographic registry of the facets over macroscopic distances is ensured, because the sapphire is a single crystal (*14*). There are, though, dislocations and an ~26% variation in the pitch, randomly located across the surface.

Five different polystyrene-*block*-poly(ethylene oxides) (PS-*b*-PEOs), with number-average molecular weights (M_n) from 7 to 43.0 kg/mol, polystyrene-*block*-poly(2-vinylpyridine) (PS-*b*-P2VP) (M_n = 19.5 kg/mol), and PS-*b*-P4VP (M_n = 19 kg/mol), all with narrow molecular weight distributions and minor volume fractions of ~0.3, were used (SOM, section S1). In the bulk, these BCPs microphase-separate into hexagonal arrays of cylindrical microdomains of PEO, P2VP or P4VP in a PS matrix. Thin films of the BCPs were spin-coated onto the faceted surfaces, which were cleaned with oxygen plasma (SOM, section S1).

Shown in Fig. 1E is a solvent-annealed, 24-nm-thick (as measured on a flat surface) film of PS-*b*-PEO (M_n = 43.0 kg/mol) on a sapphire surface, with facets having an average pitch of 130 nm and amplitude of 14 nm. Upon solvent annealing, the film is sufficiently thin that the copolymer is entrained into and confined within the regions between the facets. The solvent annealing process orients and orders the PS-*b*-PEO (*15*), but the average period is 23 nm, much less than the 29.5-nm period seen for this copolymer solvent annealed on a smooth surface. Consequently, the confinement causes a reduction in the fundamental period of the copolymer, as seen in studies of copolymers confined between planar surfaces (*16*–*18*) or within lithographically generated surface patterns (*19*). The facets essentially isolate strips of the copolymer across the surface.

With increasing film thickness, the amount of copolymer within each sawtooth increases, effectively reducing the amount of lateral confinement, which gives rise to the observed increase in the repeat period of the copolymer (SOM, section S2). When the film is sufficiently thick, as shown in Fig. 1F for a 34-nm-thick film of the same copolymer on a surface with facets having a pitch of 100 nm and amplitude of 10 nm, solvent annealing generates a single hexagonal array of cylindrical microdomains oriented normal to the film surface, with an average period of

[1]Department of Polymer Science and Engineering, University of Massachusetts, Amherst, MA 01003, USA. [2]Department of Materials Science and Engineering, Yonsei University, Seoul 120-749, Korea. [3]Department of Materials Science and Engineering, Department of Chemistry, University of Berkeley, and Material Sciences Division, Lawrence Berkeley National Laboratory, Berkeley, CA 94720, USA.

*Present address: School of Nano Bio Chemical Engineering, Ulsan National Institute of Science and Technology, BanYeon-Ri 194, Ulsan 689-805, Korea.

†To whom correspondence should be addressed. E-mail: russell@mail.pse.umass.edu (T.P.R.); tingxu@berkeley.edu (T.X.)

29.5 nm, equal to that of the copolymer solvent annealed on a planar surface. A single array covers the entire surface, where the (10) planes of the hexagonal array run parallel to the edges of the facets, which preferentially divide two adjacent (10) planes. This orientation of the hexagonal array minimizes perturbations of the lateral packing of the BCP chains and the deformation of the chains at the substrate (SOM, section S2). Because the BCP film is continuous across the edges, the lateral ordering, as opposed to the substrate topography, determines the exact placement of the microdomains, because the entropic penalty is less than that if the BCP were to follow the substrate topography exactly. Consequently, defects in the lateral packing of the microdomains that arise from the substrate topography are healed by the lateral assembly. Thus, a single copolymer array with a high degree of lateral order is produced, in which the orientation of the lattice is guided by the substrate topography. Consequently, the period of the copolymer, L, and the pitch of the substrate topography, L_S, must not be equal. We used L_S/L ratios of up to 3 without degrading the lateral ordering. If the thickness of the film relative to the amplitude of the facets is too large, the substrate no longer guides the lateral ordering, and results similar to those of films generated on a planar surface are found (SOM, section S2).

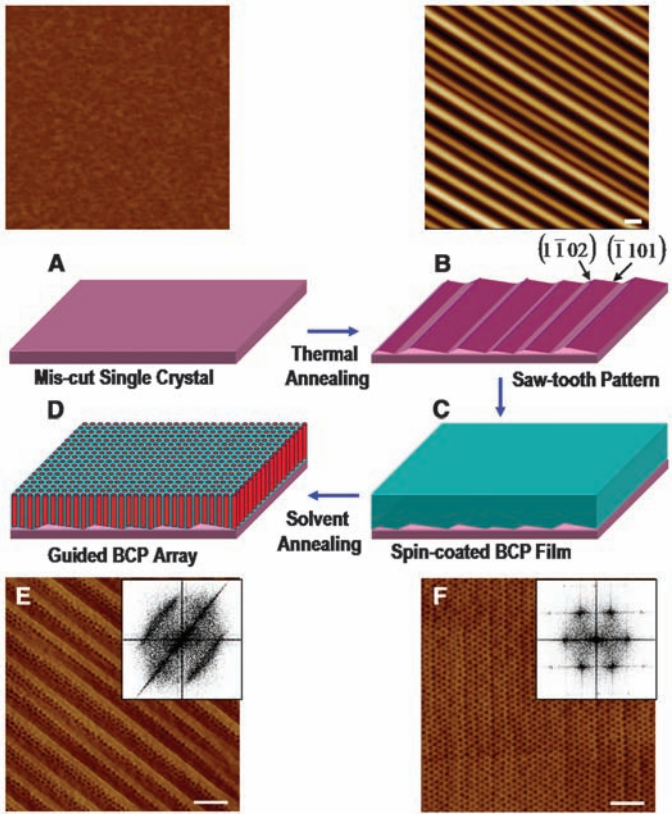

Fig. 1. Schematic illustration of the strategy used for generating BCP cylindrical microdomains on highly oriented crystalline facets on a single-crystal surface. Here, the M-plane sapphire (**A**) was annealed in air at 1300° to 1500°C for 24 hours to form sawtooth patterns. (**B**) Upon thermal annealing, the flat surface of the M-plane sapphire reconstructs into facets with the $(\bar{1}101)$ and $(1\bar{1}02)$ planes on opposite edges. (**C**) Smooth PS-*b*-PEO (M_n = 43.0 kg/mol) thin films were spin-coated onto these surfaces that, upon annealing in o-xylene vapors (**D**), produced highly ordered cylindrical microdomains oriented normal to the film surface. AFM height images of the substrate at each step are shown at the top. (**E** and **F**) AFM phase images of solvent-annealed PS-*b*-PEO (M_n = 43.0 kg/mol) films with thicknesses of (E) 24 nm and (F) 34 nm on a surfaces with facets having pitches of 130 and 100 nm with amplitudes of 14 and 10 nm. Scale bars, 200 nm.

Figure 2, A and D, show AFM images of two faceted sapphire surfaces along with thin films of four different PS-*b*-PEOs. These are M-plane sapphire surfaces annealed at 1400° and 1500°C in air for 24 hours with facet pitches of ~48 and ~24 nm and amplitudes of ~6 and ~3 nm, respectively. Figure 2, B and C, show AFM height images of ~43.5- and ~41.2-nm-thick films of PS-*b*-PEO (M_n = 26.5 kg/mol and M_n = 25.4 kg/mol, respectively), that were spin-coated and solvent-annealed in o-xylene on the surface shown in Fig. 2A, whereas Fig. 2, E and F, show AFM height images of ~30.6- and ~20.0-nm-thick films of PS-*b*-PEO (M_n = 21.0 kg/mol) and Au salt-complexed PS-*b*-PEO (M_n = 7.0 kg/mol) that were prepared on the surface in Fig. 2D. Au complexation was used to induce the microphase separation of the PS-*b*-PEO (M_n = 7.0 kg/mol), which is otherwise phase-mixed in the bulk (SOM, section S1). In all cases, regardless of the position on a 1.5 × 1.5 cm^2 sapphire wafer, the solvent-annealed films show lateral ordering of the hexagonally packed cylindrical microdomains over the entire area scanned (2 × 2 μm). The facets on the substrate do not confine the BCP laterally or influence its period. The Fourier transform of the AFM images in Fig. 2, B and C, show multiple higher-order interferences characteristic of the long-range ordering of the cylindrical microdomain arrays that are aligned with the facets on the substrate. Moiré patterns (*20*), which are interference patterns produced by overlaying a reference grating on the AFM image, show a single grain of the cylindrical microdomains over 25 × 25 μm^2 areas for PS-*b*-PEO on the faceted sapphire surface in Fig. 2D (SOM, fig. S4). From the AFM image, an orientational order parameter (SOM, section S4) of 0.93 is found that does not decay. An algebraically decaying correlation function of the translational order with an exponent of 0.32 (SOM, section S5) is found,

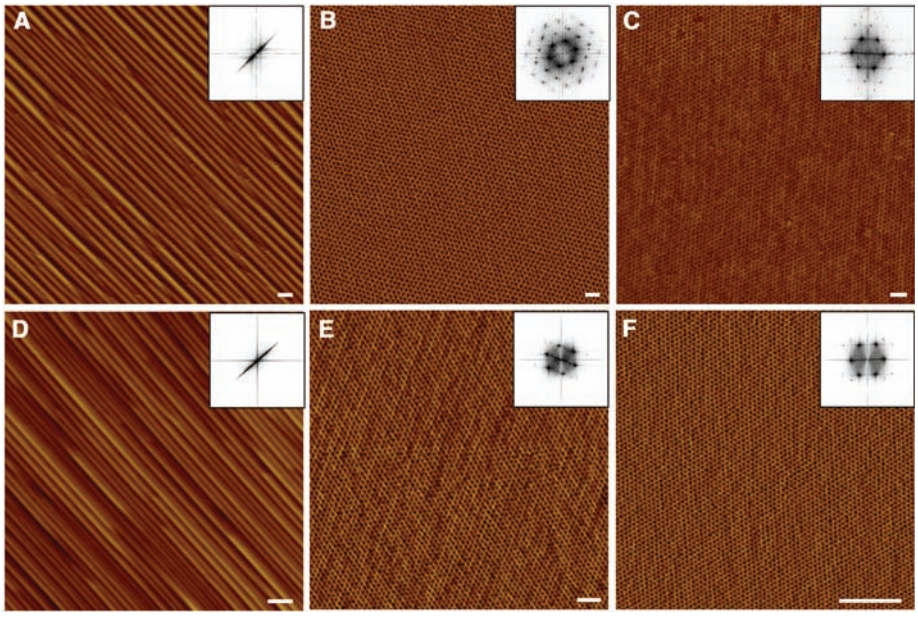

Fig. 2. AFM height images of sawtooth patterns and phase images of solvent-annealed PS-*b*-PEO thin films. (**A** and **D**) When M-plane sapphire was annealed at 1400° and 1500°C, a pitch of ~48 and ~24 nm and a peak-to-valley depth of ~6 and ~3 nm were obtained, respectively. Highly ordered PEO cylindrical microdomains having areal densities of 0.74 to 10.5 terabit/$inch^2$ from PS-*b*-PEO (M_n = 26.5 kg/mol) (**B**), PS-*b*-PEO (M_n = 25.4 kg/mol) (**C**), PS-*b*-PEO (M_n = 21.0 kg/mol) (**E**), and PS-*b*-PEO (M_n = 7.0 kg/mol) (**F**) BCP thin films annealed in o-xylene vapor were obtained. Scale bars, 100 nm.

characteristic of quasi–long-range crystalline order (*21*). Feature sizes ranging from 13 to 3 nm, with lattice spacings from 30.2 to 6.9 nm, respectively, are shown in Fig. 2 that correspond to areal densities of the microdomains from 0.74 to 10.5 terabit/inch^2. With decreasing size and period of the BCP microdomains, the orientational order and translational order were found to be improved. Similar results were also obtained with PS-*b*-P2VP and PS-*b*-P4VP, underscoring the generality of this approach (SOM, fig. S9, A and B).

Although AFM characterizes the local ordering of the microdomains (typically 20 × 20 μm), characterization of the ordering on the nanoscopic level over macroscopic length scales is required. Grazing incidence small-angle x-ray scattering (GISAXS) (SOM, section S6), in which x-rays impinge on the surface of the film at very small angles, was used to characterize the nanoscopic ordering of the BCP thin films over macroscopic distances, because the footprint of the x-ray beam is ~2 cm in length across the surface (*22*, *23*). At incidence angles above the critical angle of the polymer (~0.16°) but below the critical angle of sapphire (~0.28°), the x-rays penetrate into the polymer film and are totally reflected at the sapphire interface. When PS-*b*-PEO (M_n = 26.5 kg/mol) was solvent-annealed in a benzene and water environment, the sizes and separation distances of the cylindrical microdomains were larger than those seen in the bulk, because solvent annealing leaves the BCP film in a nonequilibrium (though highly reproducible) state (*15*, *24*). PS-*b*-PEO (M_n = 26.5 kg/mol) shows an average center-to-center distance between the cylindrical microdomains of 63.5 nm, whereas the center-to-center distance in the bulk is 36.5 nm. By rotating the film about the surface normal, discrete directions were found that corresponded to specific lattice lines of a two-dimensional (2D) hexagonal array. The sample was aligned so that the direction of the x-ray beam coincided with the (10) plane of the hexagonal array (schematically shown in the insets of Fig. 3) to collect the GISAXS pattern in Fig. 3A. Bragg rods (reflections along the horizon that are extended in the vertical) are seen at scattering vectors characteristic of the (*h*,0) planes, where *h* is an integer, of a hexagonal array of cylindrical microdomains oriented normal to the surface that are truncated at the surface (*25*). A line scan along the horizon is shown in the inset. No evidence of (*hk*) reflections, where *k* is nonzero, is observed, indicating that there is no misorientation of the lattice over the area sampled by the beam (that is, the BCP array consists of a single grain). When the sample is rotated 30° (schematically shown in the inset of Fig. 3B), Bragg rods are seen at scattering vectors corresponding to the (10), (11), (20), (21), (30), etc. planes characteristic of a hexagonal array of cylinders oriented normal to the film surface (Fig. 3B). A line scan along the horizon is shown in the inset. When the sample is rotated 30° further (Fig. 3C), only (*h*,0) reflections are seen and another 30° rotation (Fig. 3D) shows an orientation identical to that in Fig. 3B. Because only (*h*,0) reflections at three views separated by 60° from a known hexagonal array, we conclude that the film contains a single hexagonal array with no grains or misorientations of the lattice over macroscopic length scales; that is, the in-plane orientational ordering is perfect over the entire surface (~4 cm^2 of area).

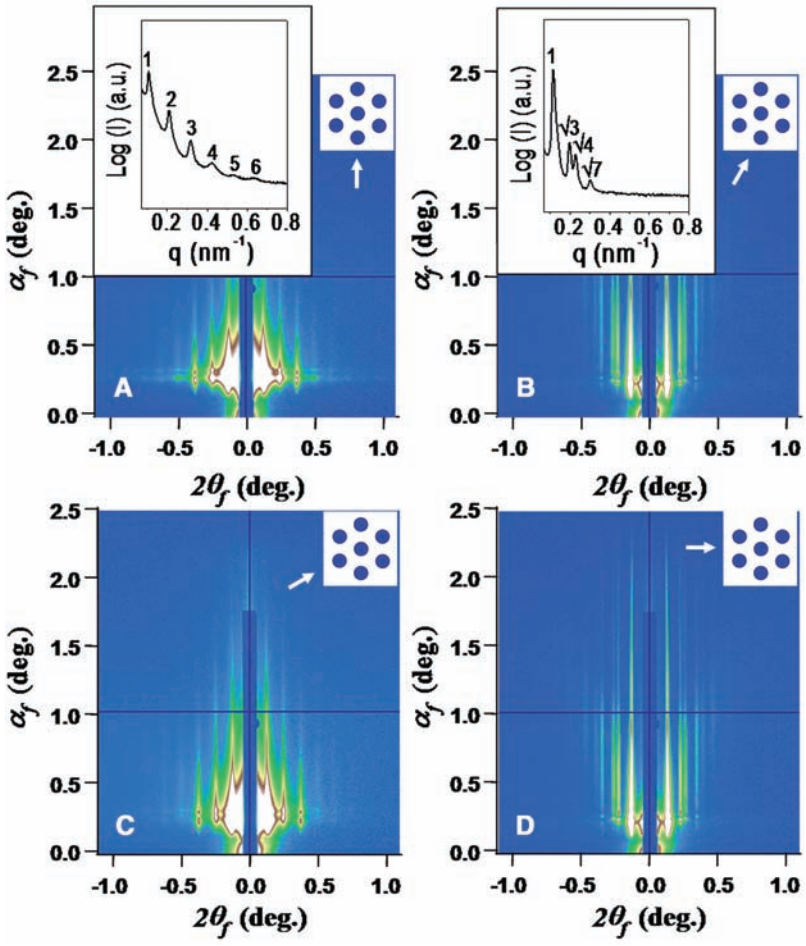

Fig. 3. Schematic 2D hexagonal lattices (insets at right) and the GISAXS patterns of PS-*b*-PEO thin films annealed in benzene and water vapors. (**A** and **C**) Integer-order diffraction peaks are shown from GISAXS patterns of cylindrical microdomains, when the x-ray beam follows the (10) lattice line (0° or 60°). (**B** and **D**) When the sample stage is rotated to 30° or 90° from this position (schematic in insets), diffraction peaks from (11) and (21) lattice lines are seen. Line profiles of the scattering as a function of the scattering vector are shown in the insets at left in (A) and (B). θ_f, in-plane scattering angle; *q*, in-plane scattering vector; a.u., arbitrary units.

The reconstruction of BCP thin films by immersion in a good solvent for the minor component but a nonsolvent for the matrix was used to convert the BCP films into nanoporous films in which the diameter of the pores is commensurate with the original diameter of the cylindrical microdomains (*25*, *26*). For films of PS-based BCPs with PEO, P2VP, and P4VP cylindrical microdomains, if the film's thickness corresponds to one period, then immersion in ethanol produces ultrahigh-density nanoporous films (SOM, fig. S9, A and B) that are ideal templates and scaffolds for the fabrication of ordered nanoscopic arrays of inorganic materials suitable for device applications (*25*, *27*).

On any single-crystalline substrate, there will be defects such as dislocations in the facets on the reconstructed surface. These defects are not seen in the BCP microdomain arrays. Shown in Fig. 4A is a 40-nm-thick film of PS-*b*-PEO (M_n = 26.5 kg/mol) with a highly ordered hexagonal array of cylinders oriented normal to the surface. The image of Fig. 4B was taken by translating the sample by ~2 μm. A piece of the film was removed from the surface, revealing the underlying substrate. One dislocation (indicated by an arrow in Fig. 4A) was located on the uncovered area that served as a marker. Subsequently, the entire PS-*b*-PEO film was removed by thoroughly rinsing the substrate with benzene. AFM images of the cleaned sapphire surface are shown in Fig. 4D and, with the sample translated by ~2 μm, in Fig. 4E. The marker dislocation was identified (indicated by an arrow in Fig. 4D) and, even though the sapphire surface shown in Fig. 4, D and E, contained many dislocations (circled in Fig. 4F, the black and white image of Fig. 4E), the ordering of the copolymer film shown in Fig. 4B, taken over the same area as in Fig. 4D, was unperturbed. A Voronoi diagram (*21*) of the data in Fig. 4B is shown in Fig. 4C, where only a single bound pair of defects is seen (SOM,

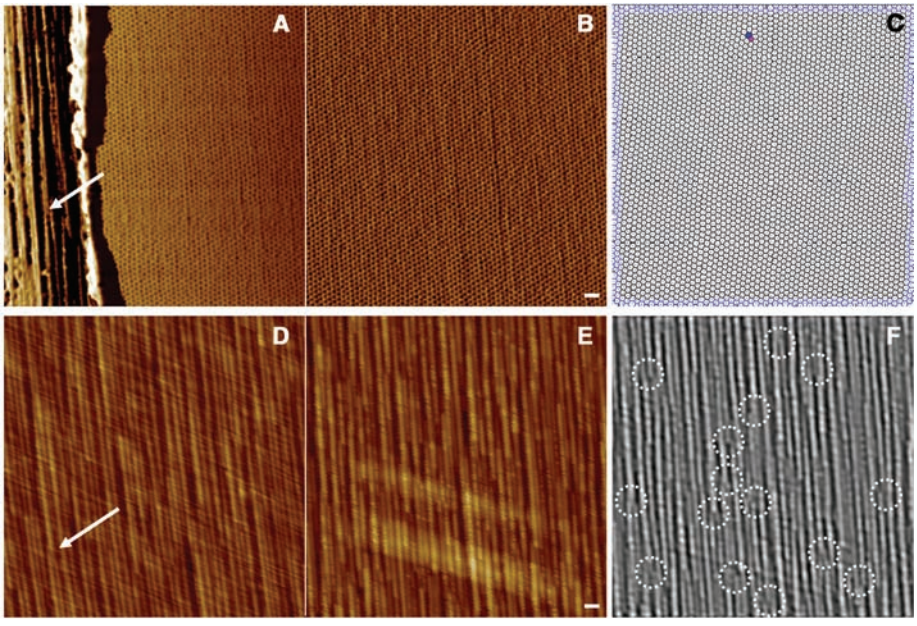

Fig. 4. (**A**) AFM height images of solvent-annealed PS-*b*-PEO (M_n = 26.5 kg/mol) thin films. To reveal the underlying substrates, a strip of the film was scratched from the surface and a dislocation (indicated by an arrow) was identified. (**B**) AFM image of a region shifted by ~2 μm from the image in (A). (**C**) The corresponding Voronoi construction of (B). (**D** and **E**) AFM images of the substrate surface after removal of the BCP film with the same dislocation in (A) indicated by the arrow in (D). (**F**) AFM image of the substrate underneath the BCP film from which the Voronoi diagram was constructed, with dotted circles indicating some of the dislocations. Scale bars, 100 nm.

section S8). This pair of defects is not associated with any defect on the underlying substrate but originates from the BCP self-assembly. These results show that the BCP self-assembly does not follow the substrate defects and that the BCP self-assembly overrides these defects.

We have demonstrated a very simple, general route to obtain highly ordered ultradense arrays in BCP films over macroscopic distances using faceted surfaces of commercially available single-crystal sapphire substrates. Despite defects in the surface topography, such as dislocations and a distribution of pitches, the BCPs self-assemble into hexagonal arrays of cylindrical microdomains oriented normal to the film surface with essentially perfect orientational order and a quasi–long-range crystalline order. The self-assembly overrides substrate defects and uses the topography only as a guide to the orientation of the arrays. Arrays of 3-nm-diameter cylindrical microdomains oriented normal to the film surface with a center-to-center distance of 6.9 nm (that is, having areal densities in excess of 10 terabit/inch^2), which is at least an order of magnitude over current capabilities, have been produced. These BCP films are promising candidates for the generation of ultrahigh-density media that have the potential of being addressable.

References and Notes

1. G. H. Fredrickson, F. S. Bates, *Annu. Rev. Mater. Sci.* **26**, 501 (1996).
2. F. S. Bates, G. H. Fredrickson, *Phys. Today* **52**, 32 (1999).
3. C. J. Hawker, T. P. Russell, *MRS Bull.* **30**, 952 (2005).
4. R. Ruiz *et al.*, *Science* **321**, 936 (2008).
5. I. Bita *et al.*, *Science* **321**, 939 (2008).
6. C. Tang *et al.*, *Science* **322**, 429 (2008).
7. M. Lazzari, G. Liu, S. Lecommandoux, *Block Copolymers in Nanoscience* (Wiley-VCH, Weinheim, Germany, 2006), chap. 9.
8. R. A. Segalman, H. Yokoyama, E. J. Kramer, *Adv. Mater.* **13**, 1152 (2001).
9. J. Y. Cheng, A. M. Mayes, C. A. Ross, *Nat. Mater.* **3**, 823 (2004).
10. H.-W. Li, W. T. S. Huck, *Nano Lett.* **4**, 1633 (2004).
11. C. L. Soles, Y. Ding, *Science* **322**, 689 (2008).
12. L. Rockford *et al.*, *Phys. Rev. Lett.* **82**, 2602 (1999).
13. M. Huth *et al.*, *Adv. Funct. Mater.* **12**, 333 (2002).
14. R. Gabai, A. Ismach, E. Joselevich, *Adv. Mater.* **19**, 1325 (2007).
15. S. H. Kim, M. J. Misner, T. Xu, M. Kimura, T. P. Russell, *Adv. Mater.* **16**, 226 (2004).
16. D. G. Walton *et al.*, *Macromolecules* **27**, 6225 (1994).
17. M. J. Fasolka *et al.*, *Phys. Rev. Lett.* **79**, 3018 (1997).
18. P. Lambooy *et al.*, *Phys. Rev. Lett.* **72**, 2899 (1994).
19. J. Y. Cheng, A. M. Mayes, C. A. Ross, *Nat. Mater.* **3**, 823 (2004).
20. A. Hexemer, G. E. Stein, E. J. Kramer, S. Magonov, *Macromolecules* **38**, 7083 (2005).
21. R. A. Segalman, A. Hexemer, R. C. Hayward, E. J. Kramer, *Macromolecules* **36**, 3272 (2003).
22. B. Lee *et al.*, *Macromolecules* **38**, 4311 (2005).
23. G. E. Stein, E. J. Kramer, X. Li, J. Wang, *Phys. Rev. Lett.* **98**, 086101 (2007).
24. S. Park, J.-Y. Wang, B. Kim, J. Xu, T. P. Russell, *ACS Nano* **2**, 766 (2008).
25. S. Park, J.-Y. Wang, B. Kim, T. P. Russell, *Nano Lett.* **8**, 1667 (2008).
26. T. Xu *et al.*, *Adv. Funct. Mater.* **13**, 698 (2003).
27. S. Park, B. Kim, J.-Y. Wang, T. P. Russell, *Adv. Mater.* **20**, 681 (2008).
28. This work was supported by the U.S. Department of Energy (DOE) under contracts DE-FG-0296ER45612 (to T.P.R., S.P., and S.H.), DE-FG-0296ER42126 (T.P.R.), and DE-AC02-05CH11231 (T.X.); by the NSF-supported Materials Research Science and Engineering Center [DMR-0820506 (J.X. and B.K.); and by the Nanoscale Science and Engineering Center (DMI-0531171 (D.L.)] at the University of Massachusetts, Amherst. Use of the Advanced Light Source, Berkeley National Laboratory, was supported by the DOE, Office of Science, Office of Basic Energy Sciences under contract DE-AC02-05CH11231. U.J. acknowledges the support of the Korea Science and Engineering Foundation through grant R11-2007-050-02004-0. The authors are also most indebted to the insightful comments of one referee whose persistence substantially enhanced our arguments.

Supporting Online Material

www.sciencemag.org/cgi/content/full/323/5917/1030/DC1
SOM Text
Figs. S1 to S9
Table S1
References

5 November 2008; accepted 15 January 2009
10.1126/science.1168108

The Formation of Warm Dense Matter: Experimental Evidence for Electronic Bond Hardening in Gold

Ralph Ernstorfer,* Maher Harb, Christoph T. Hebeisen, Germán Sciaini, Thibault Dartigalongue, R. J. Dwayne Miller†

Under strong optical excitation conditions, it is possible to create highly nonequilibrium states of matter. The nuclear response is determined by the rate of energy transfer from the excited electrons to the nuclei and the instantaneous effect of change in electron distribution on the interatomic potential energy landscape. We used femtosecond electron diffraction to follow the structural evolution of strongly excited gold under these transient electronic conditions. Generally, materials become softer with excitation. In contrast, the rate of disordering of the gold lattice is found to be retarded at excitation levels up to 2.85 megajoules per kilogram with respect to the degree of lattice heating, which is indicative of increased lattice stability at high effective electronic temperatures, a predicted effect that illustrates the strong correlation between electronic structure and lattice bonding.

Photo-induced structural dynamics of crystals have been extensively studied with the use of femtosecond spectroscopic methods based on all-optical pump-probe techniques. Although this approach can probe the electronic response of metals and semiconductors to optical excitation with high time and energy resolution, it only provides indirect information on the nu-